

# The computation aspects of the equivalent-layer technique: review and perspective

Diego Takahashi<sup>1,\*</sup>, André L. A. Reis<sup>2</sup>, Vanderlei C. Oliveira Jr.<sup>1</sup> and Valéria C. F. Barbosa<sup>1</sup>

<sup>1</sup>*Observatório Nacional, Department of Geophysics, Rio de Janeiro, Brasil*

<sup>2</sup>*Universidade do Estado do Rio de Janeiro, Department of Applied Geology, Rio de Janeiro, Brasil*

Correspondence\*: Valéria C.F. Barbosa  
valcris@on.br

## 2 ABSTRACT

3 Equivalent-layer technique is a powerful tool for processing potential-field data in the space  
4 domain. However, the greatest hindrance for using the equivalent-layer technique is its high  
5 computational cost for processing massive data sets. The large amount of computer memory  
6 usage to store the full sensitivity matrix combined with the computational time required for matrix-  
7 vector multiplications and to solve the resulting linear system, are the main drawbacks that made  
8 unfeasible the use of the equivalent-layer technique for a long time. More recently, the advances in  
9 computational power propelled the development of methods to overcome the heavy computational  
10 cost associated with the equivalent-layer technique. We present a comprehensive review of the  
11 computation aspects concerning the equivalent-layer technique addressing how previous works  
12 have been dealt with the computational cost of this technique. Historically, the high computational  
13 cost of the equivalent-layer technique has been overcome by using a variety of strategies such as:  
14 moving data-window scheme, equivalent data concept, wavelet compression, lower-dimensional  
15 subspace, quadtree discretization, reparametrization of the equivalent layer by a piecewise-  
16 polynomial function, iterative scheme without solving a system of linear equations and the  
17 convolutional equivalent layer using the concept of block-Toeplitz Toeplitz-block (BTTB) matrices.  
18 We compute the number of floating-point operations of some of these strategies adopted in the  
19 equivalent layer technique to show their effectiveness in reducing the computational demand.  
20 Numerically, we also address the stability of some of these strategies used in the equivalent  
21 layer technique by comparing with the stability via the classic equivalent-layer technique with the  
22 zeroth-order Tikhonov regularization.

23 **Keywords:** equivalent layer, gravimetry, fast algorithms, computational cost, stability analysis

## 1 INTRODUCTION

In accord with potential theory, a continuous potential-field data (gravity and magnetic data) produced by any source can be exactly reproduced by a continuous and infinite 2D physical-property surface distribution that is called the equivalent layer. The equivalent layer is a mathematical solution of Laplace's equation in the source-free region with the observed potential-field data as the Dirichlet boundary condition (Kellogg, 1929). Grounded on well-established potential theory, the equivalent-layer technique has been used by exploration geophysicists for processing potential-field data since the late 1960s (Dampney, 1969).

Although there was always a great demand for gravity and magnetic data processing, the equivalent-layer technique has not been massively used. This occurs because its high computational cost makes the equivalent-layer technique computationally inefficient for processing massive data sets. In the classic equivalent-layer technique, the continuous problem of the equivalent layer involving integrals is approximated by a discrete form of the equivalent layer. First, a discrete and finite set of equivalent sources (point masses, prisms, magnetic dipoles, doublets) is arranged in a layer with finite horizontal dimensions and located below the observation surface. Next, a linear system of equations is set up with a large and full sensitivity matrix. Then, a regularized linear inverse problem is solved to estimate the physical property of each equivalent source within the discrete equivalent layer subject to fitting a discrete set of potential-field observations. Finally, the estimated physical-property distribution within the equivalent layer is used to accomplish the desired processing of the potential-field data (e.g., interpolation, upward/downward continuation, reduction to the pole). The latter step is done by multiplying the matrix of Green's functions associated with the desired transformation by the estimated physical-property distribution.

Beginning in the late 1980s, the equivalent-layer techniques computationally efficient have arose. To our knowledge, the first method towards improving the efficiency was proposed by Leão and Silva (1989) who used an overlapping moving-window scheme spanning the data set. The strategy adopted in Leão and Silva (1989) involves solving several smaller, regularized linear inverse problems instead of one large problem. This strategy uses a small data window and distributes equivalent sources on a small regular grid at a constant depth located below the data surface. Leão and Silva (1989) ensure that sources window extends beyond the boundaries of the data window. For each position of the data window, this scheme consists in computing the processed field at the center of the data window only and the next estimates of the processed field are obtained by shifting the data window across the entire dataset. Recently, Soler and Uieda (2021) developed a computational approach to increase the efficiency of the equivalent-layer technique by combining two strategies. The first one — the block-averaging source locations — reduces the model parameters and the second strategy — the gradient-boosted algorithm — reduces the size of the linear system to be solved by fitting the equivalent source model iteratively along overlapping windows. Notice that the equivalent-layer strategy of using a moving-window scheme either in Leão and Silva (1989) or in Soler and Uieda (2021) is similar to discrete convolution.

In another approach to reduce computational workload of the equivalent-layer technique Mendonça and Silva (1994) developed an iterative procedure by incorporating one data point at a time and thus selecting a smaller data set. This strategy adopted by Mendonça and Silva (1994) is known as 'equivalent data concept'. Li and Oldenburg (2010) transformed the full sensitivity matrix into a sparse one using the compression of the coefficient matrix via wavelet transforms based on the orthonormal compactly supported wavelets. For jointly processing the components of gravity-gradient data using the equivalent-source processing, Barnes and Lumley (2011) applied the quadtree model discretization to generate a sparse linear system of equations. Davis and Li (2011) adaptively discretized the model (quadtree model discretization) based on localized anomalies and used wavelet transforms to reduce, reordered the model parameters (Hilbert

space-filling curves) and compressed each row of the sensitivity matrix of the reordered parameter set (wavelet transforms). By using the subspace method, Mendonça (2020) reduced the dimension of the linear system of equations to be solved in the equivalent-layer technique. The subspace bases span the parameter-model space and they are constructed by applying the singular value decomposition to the matrix containing the gridded data. These strategies followed by Li and Oldenburg (2010), Barnes and Lumley (2011), Davis and Li (2011) and Mendonça (2020) may be grouped into the strategy of compression approaches to solve large linear system of equations.

Following the strategy of reparametrization of the equivalent layer, Oliveira Jr. et al. (2013) reduced the model parameters by approximating the equivalent-source layer by a piecewise-polynomial function defined on a set of user-defined small equivalent-source windows. The estimated parameters are the polynomial coefficients for each window and they are much smaller than the original number of equivalent sources. Siqueira et al. (2017) developed an iterative solution where the sensitivity matrix is transformed into a diagonal matrix with constant terms through the use of the 'excess mass criterion' and of the positive correlation between the observed gravity data and the masses on the equivalent layer. Jirigalatu and Ebbing (2019) combined the Gauss-fast Fourier transform (FFT) with Landweber's algorithm and proposed a fast equivalent-layer technique for jointly processing two-components of the gravity-gradient data. The Landweber's algorithm has some similarities with gradient-descent algorithm. The strategies worked out by Siqueira et al. (2017) and Jirigalatu and Ebbing (2019) avoid calculating the Hessian matrix and solving linear system of equations.

Recently, Takahashi et al. (2020, 2022), developed fast and effective equivalent-layer techniques for processing, respectively, gravity and magnetic data by modifying the forward modeling to estimate the physical-property distribution over the layer through a 2D discrete convolution that can be efficiently computed via 2D FFT. These methods took advantage of the Block-Toeplitz Toeplitz-block (BTTB) structure of the sensitivity matrices, allowing them to be calculated by using only their first column. In practice, the forward modeling uses a single equivalent source, which significantly reduces the required RAM memory. Takahashi et al. (2020, 2022) employed the strategy of the convolutional equivalent layer using the concept of BTTB matrices.

Here, we present a comprehensive review of

## 2 THE EQUIVALENT-LAYER TECHNIQUE

### 95 2.1 Fundamentals

96 Consider a set of  $N$  potential-field observations (gravity or magnetic data)  $d_i^o(x_i, y_i, z_i)$ ,  $i = 1, \dots, N$ ,  
 97 at the  $i$ th observation point  $(x_i, y_i, z_i)$  of a Cartesian coordinate system with  $x$ -,  $y$ - and  $z$ -axis pointing to  
 98 north, east and down, respectively. Physically, the discrete set of potential-field observations is produced by  
 99 a unknown source distribution in the subsurface. Mathematically, it represents a discrete set of a harmonic  
 100 function.

101 A standard way to deal with the classical equivalent-layer technique is approximate the observed potential-  
 102 field data by the predicted data, which in turn are produced by a fictitious layer of sources, called equivalent  
 103 layer. The equivalent layer is located below the observation surface, at depth  $z_0$  ( $z_0 > z_i$ ), and with finite  
 104 horizontal dimensions being composed by a finite discrete set of equivalent sources (e.g., point masses,  
 105 dipoles, or prisms). Mathematically, this approximation can be written in matrix notation as

$$\mathbf{d} = \mathbf{A}\mathbf{p}, \quad (1)$$

106 where  $\mathbf{d}$  is an  $N$ -dimensional predicted data vector whose  $i$ th element,  $d_i(x_i, y_i, z_i)$ ,  $i = 1, \dots, N$ , is the  
 107 predicted potential-field observation,  $\mathbf{p}$  is an  $M$ -dimensional parameter vector whose  $j$ th element  $p_j$  can be  
 108 a physical property of the  $j$ th equivalent source and  $\mathbf{A}$  is the  $N \times M$  sensitivity matrix whose  $ij$ th element  
 109  $a_{ij}$  is a harmonic function.

### 110 2.2 Computational strategies

111 The classical equivalent-layer technique consists of estimating the parameter vector  $\mathbf{p}$  from the  $N$ -  
 112 dimensional observed data vector  $\mathbf{d}^o$  whose  $i$ th element is defined as the  $d_i^o(x_i, y_i, z_i)$ ,  $i = 1, \dots, N$ .  
 113 Usually, this estimate can be obtained by a regularized least-squares solution. The estimated parameter  
 114 is stable, fits the observed data and can be used to yield a desired linear transformation of the data, such  
 115 as interpolation, upward (or downward) continuation, reduction to the pole, joint processing of gravity  
 116 gradient data and more. Mathematically, the desired linear transformation of the data can be obtained by

$$\hat{\mathbf{t}} = \mathbf{T}\mathbf{p}^*, \quad (2)$$

117 where  $\hat{\mathbf{t}}$  is an  $N$ -dimensional transformed data vector,  $\mathbf{p}^*$  is an  $M$ -dimensional estimated parameter vector  
 118 and  $\mathbf{T}$  is the  $N \times M$  matrix of Green's functions whose  $ij$ th element is the transformed field at the  $i$ th  
 119 observation point produced by the  $j$ th equivalent source.

120 The biggest hurdle to use the classical equivalent-layer technique is the computational complexity  
 121 to handle large datasets because the sensitivity matrix  $\mathbf{A}$  (equation 1) is dense. Usually, the estimated  
 122 parameter vector  $\mathbf{p}^*$  requires to solve a large-scale linear inversion which in turn means to deal with  
 123 some obstacles concerning large computational cost: i) the large computer memory to store large and full  
 124 matrices; ii) the long computation time to multiply a matrix by a vector; and iii) the long computation time  
 125 to solve a large linear system of equations.

126 Here, we review some strategies for reducing the computational cost of equivalent-layer technique. These  
 127 strategies are the following:

## 128 2.2.1 The moving data-window scheme

129 Leão and Silva (1989) reduced the total processing time and memory usage of equivalent-layer technique  
 130 by means of a moving data-window scheme. A small moving data window with  $N_w$  observations and  
 131 a small equivalent layer with  $M_w$  equivalent sources ( $M_w > N_w$ ) located below the observations are  
 132 established. For each position of a moving-data window, Leão and Silva (1989) estimate a stable solution  
 133  $\mathbf{p}_w^*$  by using a data-space approach with the zeroth-order Tikhonov regularization (Aster et al., 2018), i.e.,

$$\left( \mathbf{A}_w \mathbf{A}_w^\top + \mu \mathbf{I} \right) \mathbf{w} = \mathbf{d}_w^o, \quad (3a)$$

$$\mathbf{A}_w^\top \mathbf{w} = \mathbf{p}_w^*, \quad (3b)$$

134 where  $\mathbf{w}$  is a dummy vector,  $\mu$  is a regularizing parameter,  $\mathbf{d}_w^o$  is an  $N_w$ -dimensional vector containing  
 135 the observed potential-field data,  $\mathbf{A}_w$  is an  $N_w \times M_w$  sensitivity matrix related to a moving-data window,  $\mathbf{I}$   
 136 is an identity matrix of order  $N_w$  and the superscript  $\top$  stands for a transpose. After estimating an  $M_w \times 1$   
 137 parameter vector  $\mathbf{p}_w^*$  (equation 3b) the desired transformation of the data is only calculated at the central  
 138 point of each moving-data window, i.e.:

$$\hat{\mathbf{t}}_k = \mathbf{t}_k^\top \mathbf{p}_w^*, \quad (4)$$

139 where  $\hat{\mathbf{t}}_k$  is the transformed data calculated at the central point  $k$  of the data window and  $\mathbf{t}_k$  is an  $M_w \times 1$   
 140 vector whose elements form the  $k$ th row of the  $N_w \times N_w$  matrix of Green's functions  $\mathbf{T}$  (equation 2) of the  
 141 desired linear transformation of the data.

142 By shifting the moving-data window with a shift size of one data spacing, a new position of a data  
 143 window is set up. Next, the aforementioned process (equations 3b and 4) is repeated for each position of a  
 144 moving-data window, until the entire data have been processed. Hence, instead of solving a large inverse  
 145 problem, Leão and Silva (1989) solve several much smaller ones.

146 To reduce the size of the linear system to be solved, Soler and Uieda (2021) adopted the same strategy  
 147 proposed, originally, by Leão and Silva (1989) of using a small moving-data window sweeping the whole  
 148 data. In Leão and Silva (1989), a moving-data window slides to the next adjacent data window following a  
 149 sequential movement, the predicted data is calculated inside the data window and the desired transformation  
 150 are only calculated at the center of the moving-data window. Unlike Leão and Silva (1989), Soler and  
 151 Uieda (2021) do not adopt a sequential order of the data windows; rather, they adopt a randomized  
 152 order of windows in the iterations of the gradient-boosting algorithm (Friedman, 2001 and 2002). The  
 153 gradient-boosting algorithm in Soler and Uieda (2021) estimates a stable solution using the data and the  
 154 equivalent sources that fall within a moving-data window; however, it calculates the predicted data and the  
 155 residual data in the whole survey data. Next, the residual data that fall within a new position of the data  
 156 window is used as input data to estimate a new stable solution within the data window which in turn is  
 157 used to calculate a new predicted data and a new residual data in the whole survey data. Finally, unlike  
 158 Leão and Silva (1989), in Soler and Uieda (2021) neither the data nor the equivalent sources need to be  
 159 distributed in regular grids. Indeed, Leão and Silva (1989) built their method using regular grids, but in fact  
 160 regular grids are not necessary. Regarding the equivalent-source layout, Soler and Uieda (2021) proposed  
 161 the block-averaged sources locations in which the survey area is divided into horizontal blocks and one  
 162 single equivalent source is assigned to each block. Each single source per block is placed over the layer  
 163 with its horizontal coordinates given by the average horizontal positions of observation points. According  
 164 to Soler and Uieda (2021), the block-averaged sources layout reduces the number of equivalent sources  
 165 significantly and the gradient-boosting algorithm provides even greater efficiency in terms of data fitting.

## 166 2.2.2 The equivalent-data concept

167 To reduced the total processing time and memory usage of equivalent-layer technique, Mendonça and  
 168 Silva (1994) proposed a strategy called 'equivalent data concept'. The equivalent data concept is grounded  
 169 on the principle that there is a subset of redundant data that does not contribute to the final solution and  
 170 thus can be dispensed. Conversely, there is a subset of observations, called equivalent data, that contributes  
 171 effectively to the final solution and fits the remaining observations (redundant data). Iteractively, Mendonça  
 172 and Silva (1994) selected the subset of equivalent data that is substantially smaller than the original dataset.  
 173 This selection is carried out by incorporating one data point at a time.

174 According to Mendonça and Silva (1994), the number of equivalent data is about one-tenth of the total  
 175 number of observations. These authors used the equivalent data concept to carry out an interpolation of  
 176 gravity data. They showed a reduction of the total processing time and memory usage by, at least, two  
 177 orders of magnitude as opposed to using all observations in the interpolation process via the classical  
 178 equivalent-layer technique.

## 179 2.2.3 The wavelet compression and lower-dimensional subspace

180 For large data sets, the sensitivity matrix  $\mathbf{A}$  (equation 1) is a drawback in applying the equivalent-layer  
 181 technique because it is a large and dense matrix.

182 Li and Oldenburg (2010) transformed a large and full sensitivity matrix into a sparse one by using fast  
 183 wavelet transforms. In the wavelet domain, Li and Oldenburg (2010) applyied a 2D wavelet transform to  
 184 each row and column of the original sensitivity matrix  $\mathbf{A}$  to expand it in the wavelet bases. This operation  
 185 can be done by premultiplying the original sensitivity matrix  $\mathbf{A}$  by a matrix representing the 2D wavelet  
 186 transform  $\mathbf{W}_2$  and then the resulting is postmultiplied by the transpose of  $\mathbf{W}_2$  (i.e.,  $\mathbf{W}_2^\top$ ).

$$\tilde{\mathbf{A}} = \mathbf{W}_2 \mathbf{A} \mathbf{W}_2^\top, \quad (5)$$

187 where  $\tilde{\mathbf{A}}$  is the expanded original sensitivity matrix in the wavelet bases with many elements zero or close  
 188 to zero. Next, the matrix  $\tilde{\mathbf{A}}$  is replaced by its sparse version  $\tilde{\mathbf{A}}_s$  in the wavelet domain which in turn is  
 189 obtained by retaining only the large elements of the  $\tilde{\mathbf{A}}$ . Thus, the elements of  $\tilde{\mathbf{A}}$  whose amplitudes fall  
 190 below a relative threshold are discarded. In Li and Oldenburg (2010), the original sensitivity matrix  $\mathbf{A}$   
 191 is high compressed resulting in a sparce matrix  $\tilde{\mathbf{A}}_s$  with a few percent of nonzero elements and the the  
 192 inverse problem is solved in the wavelet domain by using  $\tilde{\mathbf{A}}_s$  and a incomplete conjugate gradient least  
 193 squares, without an explicit regularization parameter and a limited number of iterations. The solution is  
 194 obtained by solving the following linear system

$$\tilde{\mathbf{A}}_L^\top \tilde{\mathbf{A}}_L \tilde{\mathbf{p}}_L^* = \tilde{\mathbf{A}}_L^\top \tilde{\mathbf{d}}^o, \quad (6)$$

195 where  $\tilde{\mathbf{p}}_L^*$  is obtained by solving the linear system given by equation 6,

$$\tilde{\mathbf{A}}_L = \tilde{\mathbf{A}}_s \tilde{\mathbf{L}}^{-1}, \quad (7a)$$

$$\tilde{\mathbf{p}}_L = \tilde{\mathbf{L}} \tilde{\mathbf{p}}, \quad (7b)$$

$$\tilde{\mathbf{d}}^o = \mathbf{W}_2 \mathbf{d}^o, \quad (7c)$$

196 where  $\tilde{\mathbf{L}}$  is a diagonal and invertible weighting matrix representing the finite-difference approximation in  
 197 the wavelet domain. Finally, the distribution over the equivalent layer in the space domain  $\mathbf{p}$  is obtained by

198 applying an inverse wavelet transform in two steps, i.e.:

$$\tilde{\mathbf{p}} = \tilde{\mathbf{L}}^{-1} \tilde{\mathbf{p}}_{\mathbf{L}}^*, \quad (8)$$

199 and

$$\mathbf{p} = \mathbf{W}_2 \tilde{\mathbf{p}}. \quad (9)$$

200 Although the data misfit quantifying the difference between the observed and predicted data by the  
201 equivalent source is calculated in the wavelet domain, we understand that the desired transformation is  
202 calculated via equation 2 which uses a full matrix of Green's functions  $\mathbf{T}$ .

203 Li and Oldenburg (2010) used the equivalent-layer technique with a wavelet compression to perform an  
204 upward continuation of total-field anomaly between uneven surfaces. For regularly spaced grid of data, Li  
205 and Oldenburg (2010) reported that high compression ratios are achieved with insignificant loss of accuracy.  
206 As compared to the upward-continued total-field anomaly by equivalent layer using the dense matrix, Li  
207 and Oldenburg's (2010) approach, using the Daubechies wavelet, decreased CPU (central processing unit)  
208 time by up to two orders of magnitude.

209 Mendonça (2020) overcame the solution of intractable large-scale equivalent-layer problem by using the  
210 subspace method (e.g., Skilling and Bryan, 1984; Kennett et al., 1988; Oldenburg et al., 1993; Barbosa  
211 et al., 1997). The subspace method reduces the dimension of the linear system of equations to be solved.  
212 Given a higher-dimensional space (e.g.,  $M$ -dimensional model space,  $\mathbb{R}^M$ ), there exists many lower-  
213 dimensional subspaces (e.g.,  $Q$ -dimensional subspace) of  $\mathbb{R}^M$ . The linear inverse problem related to the  
214 equivalent-layer technique consists in finding an  $M$ -dimension parameter vector  $\mathbf{p} \in \mathbb{R}^M$  which adequately  
215 fits the potential-field data. The subspace method looks for a parameter vector who lies in a  $Q$ -dimensional  
216 subspace of  $\mathbb{R}^M$  which, in turn, is spanned by a set of  $Q$  vectors  $\mathbf{v}_i = 1, \dots, Q$ , where  $\mathbf{v}_i \in \mathbb{R}^M$ . In matrix  
217 notation, the parameter vector in the subspace method can be written as

$$\mathbf{p} = \mathbf{V} \boldsymbol{\alpha}, \quad (10)$$

218 where  $\mathbf{V}$  is an  $M \times Q$  matrix whose columns  $\mathbf{v}_i = 1, \dots, Q$  form a basis vectors for a subspace  $Q$  of  $\mathbb{R}^M$ .  
219 In equation 10, the parameter vector  $\mathbf{p}$  is defined as a linear combination in the space spanned by  $Q$  basis  
220 vectors  $\mathbf{v}_i = 1, \dots, Q$  and  $\boldsymbol{\alpha}$  is a  $Q$ -dimensional unknown vector to be determined. The main advantage of  
221 the subspace method is that the linear system of  $M$  equations in  $M$  unknowns to be originally solved is  
222 reduced to a new linear system of  $Q$  equations in  $Q$  unknowns which requires much less computational  
223 effort since  $Q \ll M$ , i.e.:

$$\mathbf{V}^\top \mathbf{A}^\top \mathbf{A} \mathbf{V} \boldsymbol{\alpha}^* = \mathbf{V}^\top \mathbf{d}^o. \quad (11)$$

224 To avoid the storage of matrices  $\mathbf{A}$  and  $\mathbf{V}$ , Mendonça (2020) evaluates an element of the matrix  $\mathbf{AV}$  by  
225 calculating the dot product between the row of matrix  $\mathbf{A}$  and the column of the matrix  $\mathbf{B}$ . After estimating  
226  $\boldsymbol{\alpha}^*$  (equation 11) belonging to a  $Q$ -dimensional subspace of  $\mathbb{R}^M$ , the distribution over the equivalent layer  
227  $\mathbf{p}$  in the  $\mathbb{R}^M$  is obtained by applying equation 10. The choice of the  $Q$  basis vectors  $\mathbf{v}_i = 1, \dots, Q$  (equation  
228 10) in the subspace method is not strict. Mendonça (2020), for example, chose the eigenvectors yielded by  
229 applying the singular value decomposition of the matrix containing the gridded data set. The number of  
230 eigenvectors used to form basis vectors will depend on the singular values.

231 The proposed subspace method for solving large-scale equivalent-layer problem by Mendonça (2020)  
232 was applied to estimate the mass excess or deficiency caused by causative gravity sources.

## 233 2.2.4 The quadtree discretization

234 To make the equivalent-layer technique tractable, Barnes and Lumley (2011) also transformed the dense  
 235 sensitivity matrix  $\mathbf{A}$  (equation 1) into a sparse matrix. In Barnes and Lumley (2011), a sparse version of  
 236 the sensitivity matrix is achieved by grouping equivalent sources (e.g., they used prisms) distant from an  
 237 observation point together to form a larger prism or larger block. Each larger block has averaged physical  
 238 properties and averaged top- and bottom-surfaces of the grouped smaller prisms (equivalent sources) that  
 239 are encompassed by the larger block. The authors called it the 'larger averaged block' and the essence of  
 240 their method is the reduction in the number of equivalent sources, which means a reduction in the number  
 241 of parameters to be estimated implying in model dimension reduction.

242 The key of the Barnes and Lumley's (2011) method is the algorithm for deciding how to group the smaller  
 243 prisms. In practice, these authors used a recursive bisection process that results in a quadtree discretization  
 244 of the equivalent-layer model.

245 By using the quadtree discretization, Barnes and Lumley (2011) were able to jointly process multiple  
 246 components of airborne gravity-gradient data using a single layer of equivalent sources. To our knowledge,  
 247 Barnes and Lumley (2011) are the pioneers on processing full-tensor gravity-gradient data jointly. In  
 248 addition to computational feasibility, Barnes and Lumley's (2011) method reduces low-frequency noise  
 249 and can also remove the drift in time-domain from the survey data. Those authors stressed that the  
 250  $G_{zz}$ -component calculated through the single estimated equivalent-layer model projected on a grid at a  
 251 constant elevation by inverting full gravity-gradient data has the low-frequency error reduced by a factor of  
 252 2.4 as compared to the inversion of an individual component of the gravity-gradient data.

## 253 2.2.5 The reparametrization of the equivalent layer

254 Oliveira Jr. et al. (2013) reparametrized the whole equivalent-layer model by a piecewise bivariate-  
 255 polynomial function defined on a set of  $Q$  equivalent-source windows. In Oliveira Jr. et al.'s (2013)  
 256 approach, named polynomial equivalent layer (PEL), the parameter vector within the  $k$ th equivalent-source  
 257 window  $\mathbf{p}^k$  can be written in matrix notation as

$$\mathbf{p}^k = \mathbf{B}^k \mathbf{c}^k, \quad k = 1 \dots Q, \quad (12)$$

258 where  $\mathbf{p}^k$  is an  $M_w$ -dimensional vector containing the physical-property distribution within the  $k$ th  
 259 equivalent-source window,  $\mathbf{c}^k$  is a  $P$ -dimensional vector whose  $l$ th element is the  $l$ th coefficient of the  
 260  $\alpha$ th-order polynomial function and  $\mathbf{B}^k$  is an  $M_w \times P$  matrix containing the first-order derivative of the  
 261  $\alpha$ th-order polynomial function with respect to one of the  $P$  coefficients.

262 By using a regularized potential-field inversion, Oliveira Jr. et al. (2013) estimates the polynomial  
 263 coefficients for each equivalent-source window by solving the following linear system

$$(\mathbf{B}^\top \mathbf{A}^\top \mathbf{A} \mathbf{B} + \mu \mathbf{I}) \mathbf{c}^* = \mathbf{B}^\top \mathbf{A}^\top \mathbf{d}^o, \quad (13)$$

264 where  $\mu$  is a regularizing parameter,  $\mathbf{c}^*$  is an estimated  $H$ -dimensional vector containing all coefficients  
 265 describing all polynomial functions within all equivalent-source windows which compose the entire  
 266 equivalent layer,  $\mathbf{I}$  is an identity matrix of order  $H$  ( $H = PQ$ ) and  $\mathbf{B}$  is an  $M \times H$  block diagonal matrix  
 267 such that the main-diagonal blocks are  $\mathbf{B}^k$  matrices (equation 12) and all off-diagonal blocks are zero  
 268 matrices. For ease of the explanation of equation 13, we keep only the zeroth-order Tikhonov regularization

269 and omitting the first-order Tikhonov regularization (Aster et al., 2018) which was also used by Oliveira Jr.  
 270 et al. (2013).

271 The main advantage of the PEL is solve  $H$ -dimensional system of equations (equation 13), where  $H$   
 272 totalizes the number of polynomial coefficients composing all equivalent-source windows, requiring a  
 273 lower computational effort since  $H << N$ . To avoid the storage of matrices  $\mathbf{A}$  and  $\mathbf{B}$ , Oliveira Jr. et al.  
 274 (2013) evaluate an element of the matrix  $\mathbf{AB}$  by calculating the dot product between the row of matrix  $\mathbf{A}$   
 275 and the column of the matrix  $\mathbf{B}$ . After estimating all polynomial coefficients of all windows, the estimated  
 276 coefficients ( $\mathbf{c}^*$  in equation 13) are transformed into a single physical-property distribution encompassing  
 277 the entire equivalent layer.

278 As stated by Oliveira Jr. et al. (2013), the computational efficiency of PEL approach stems from the fact  
 279 that the total number of polynomial coefficients  $H$  required to depict the physical-property distribution  
 280 within the equivalent layer is generally much smaller than the number of equivalent sources. Consequently,  
 281 this leads to a considerably smaller linear system that needs to be solved. Hence, the main strategy of  
 282 polynomial equivalent layer is the model dimension reduction.

283 The polynomial equivalent layer was applied to perform upward continuations of gravity and magnetic  
 284 data and reduction to the pole of magnetic data.

## 285 2.2.6 The iterative scheme without solving a linear system

286 There exists a class of methods that iteratively estimate the distribution of physical properties within an  
 287 equivalent layer without the need to solve linear systems. The method initially introduced by Cordell (1992)  
 288 and later expanded upon by Guspi and Novara (2009) updates the physical property of sources, located  
 289 beneath each potential-field data, by removing the maximum residual between the observed and fitted data.  
 290 In addition, Xia and Sprowl (1991) and Xia et al. (1993) have developed efficient iterative algorithms for  
 291 updating the distribution of physical properties within the equivalent layer in the wavenumber and space  
 292 domains, respectively. Specifically, in Xia and Sprowl's (1991) method the physical-property distribution is  
 293 updated by using the ratio between the squared depth to the equivalent source and the gravitational constant  
 294 multiplied by the residual between the observed and predicted observation at the measurement station.  
 295 Neither of these methods solve linear systems.

296 Following this class of methods of iterative equivalent-layer technique that does not solve linear systems,  
 297 Siqueira et al. (2017) developed a fast iterative equivalent-layer technique for processing gravity data in  
 298 which the sensitivity matrix  $\mathbf{A}$  (equation 1) is replaced by a diagonal matrix  $N \times N$ , i.e.:

$$\tilde{\mathbf{A}} = 2\pi\gamma\Delta\mathbf{S}^{-1}, \quad (14)$$

299 where  $\gamma$  is Newton's gravitational constant and  $\Delta\mathbf{S}^{-1}$  is a diagonal matrix of order  $N$  whose diagonal  
 300 elements  $\Delta s_i$ ,  $i = 1, \dots, N$  are the element of area centered at the  $i$ th horizontal coordinates of the  $i$ th  
 301 observation point. The physical foundations of Siqueira et al.'s (2017) method rely on two constraints: i) the  
 302 excess of mass; and ii) the positive correlation between the gravity observations and the mass distribution  
 303 over the equivalent layer.

304 Although Siqueira et al.'s (2017) method does not solve any linear system of equations, it can be  
 305 theoretically explained by solving the following linear system at the  $k$ th iteration:

$$\tilde{\mathbf{A}}^\top \tilde{\mathbf{A}} \Delta \hat{\mathbf{p}}^k = \tilde{\mathbf{A}}^\top \mathbf{r}^k, \quad (15)$$

306 where  $\mathbf{r}^k$  is an  $N$ -dimensional residual vector whose  $i$ th element is calculated by subtracting the  $i$ th  
 307 observed data  $d_i^o$  from the  $i$ th fitted data  $d_i^k$  at the  $k$ th iteration, i.e.,

$$r_i^k = d_i^o - d_i^k. \quad (16)$$

308 and  $\Delta \hat{\mathbf{p}}^k$  is an estimated  $N$ -dimensional vector of parameter correction.

309 Because  $\tilde{\mathbf{A}}$ , in equation 15, is a diagonal matrix (equation 14), the parameter correction estimate is  
 310 directly calculated without solving system of linear equations, and thus, an  $i$ th element of  $\Delta \hat{\mathbf{p}}^k$  is directly  
 311 calculated by

$$\Delta \hat{p}_i^k = \frac{\Delta s_i r_i^k}{2 \pi \gamma}. \quad (17)$$

312 The mass distribution over the equivalent layer is updated by:

$$\hat{p}_i^{k+1} = \hat{p}_i^k + \Delta \hat{p}_i^k. \quad (18)$$

313 Siqueira et al.'s (2017) method starts from a mass distribution on the equivalent layer, whose  $i$ th mass  $p_i^o$  is  
 314 proportional to the  $i$ th observed data  $d_i^o$ , i.e.,

$$p_i^o = \frac{\Delta s_i d_i^o}{2 \pi \gamma}. \quad (19)$$

315 Siqueira et al. (2017) applied their fast iterative equivalent-layer technique to interpolate, calculate the  
 316 horizontal components, and continue upward (or downward) gravity data.

317 For jointly process two gravity gradient components, Jirigalatu and Ebbing (2019) used the Gauss-FFT  
 318 for forward calculation of potential fields in the wavenumber domain combined with Landweber's iteration  
 319 coupled with a mask matrix  $\mathbf{M}$  to reduce the edge effects without increasing the computation cost. The  
 320 mask matrix  $\mathbf{M}$  is defined in the following way: if the corresponding pixel does not contain the original  
 321 data, the element of  $\mathbf{M}$  is set to zero; otherwise, it is set to one. The  $k$ th Landweber iteration is given by

$$\mathbf{p}_{k+1} = \mathbf{p}_k + \omega \left[ \mathbf{A}_1^\top (\mathbf{d}_1 - \mathbf{M} \mathbf{A}_1 \mathbf{p}_k) + \mathbf{A}_2^\top (\mathbf{d}_2 - \mathbf{M} \mathbf{A}_2 \mathbf{p}_k) \right], \quad (20)$$

322 where  $\omega$  is a relaxation factor,  $\mathbf{d}_1$  and  $\mathbf{d}_2$  are the two gravity gradient components and  $\mathbf{A}_1$  and  $\mathbf{A}_2$  are the  
 323 corresponding gravity gradient kernels. Jirigalatu and Ebbing (2019) applied their method for processing  
 324 two horizontal curvature components of Falcon airborne gravity gradient.

### 325 2.2.7 The convolutional equivalent layer with BTTB matrices

326 Takahashi et al. (2020, 2022) introduced the convolutional equivalent layer for gravimetric and magnetic  
 327 data processing, respectively.

328 Takahashi et al. (2020) demonstrated that the sensitivity matrix  $\mathbf{A}$  (equation 1) associated with a planar  
 329 equivalent layer formed by a set of point masses, each one directly beneath each observation point and  
 330 considering a regular grid of observation points at a constant height has a symmetric block-Toeplitz  
 331 block (BTTB) structure. A symmetric BTTB matrix has, at least, two attractive properties. The first one is  
 332 that it can be defined by using only the elements forming its first column (or row). The second attractive  
 333 property is that any BTTB matrix can be embedded into a symmetric Block-Circulant Circulant-Block

(BCCB) matrix. This means that the full sensitivity matrix  $\mathbf{A}$  (equation 1) can be completely reconstruct by using the first column of the BCCB matrix only. In what follows, Takahashi et al. (2020) computed the forward modeling by using only a single equivalent source. Specifically, it is done by calculating the eigenvalues of the BCCB matrix that can be efficiently computed by using only the first column of the BCCB matrix via 2D fast Fourier transform (2D FFT). By comparing with the classic approach in the Fourier domain, the convolutional equivalent layer for gravimetric data processing proposed by Takahashi et al. (2020) performed upward- and downward-continue gravity data with a very small border effects and noise amplification.

By using the original idea of the convolutional equivalent layer proposed by Takahashi et al. (2020) for gravimetric data processing, Takahashi et al. (2022) developed the convolutional equivalent layer for magnetic data processing. By assuming a regularly spaced grid of magnetic data at a constant height and a planar equivalent layer of dipoles, Takahashi et al. (2022) proved that the sensitivity matrix linked with this layer possess a BTTB structure in the specific scenario where each dipole is exactly beneath each observed magnetic data point. Takahashi et al. (2022) used a conjugate gradient least-squares (CGLS) algorithm which does not require an inverse matrix or matrix-matrix multiplication. Rather, it only requires matrix-vector multiplications per iteration, which can be effectively computed using the 2D FFT as a discrete convolution. The matrix-vector product only uses the elements that constitute the first column of the associated BTTB matrix, resulting in computational time and memory savings. Takahashi et al. (2022) showed the robustness of the convolutional equivalent layer in processing magnetic survey that violates the requirement of regular grids in the horizontal directions and flat observation surfaces.

The matrix-vector product in Takahashi et al. (2020, 2022) (e.g.,  $\mathbf{d} = \mathbf{Ap}$ , such as in equation 1) is the main issue to be solved. To solve it efficiently, these authors involved the auxiliary linear system

$$\mathbf{w} = \mathbf{Cv}, \quad (21)$$

where  $\mathbf{w}$  and  $\mathbf{v}$  are, respectively, vectors of data and parameters completed by zeros and  $\mathbf{C}$  is a BCCB matrix formed by  $2Q \times 2Q$  blocks, where each block  $\mathbf{C}_q$ ,  $q = 0, \dots, Q - 1$ , is a  $2P \times 2P$  circulant matrix. The first column of  $\mathbf{C}$  is obtained by rearranging the first column of the sensitivity matrix  $\mathbf{A}$  (equation 1). Because a BCCB matrix is diagonalized by the 2D unitary discrete Fourier transform (DFT),  $\mathbf{C}$  can be written as

$$\mathbf{C} = (\mathbf{F}_{2Q} \otimes \mathbf{F}_{2P})^* \boldsymbol{\Lambda} (\mathbf{F}_{2Q} \otimes \mathbf{F}_{2P}), \quad (22)$$

where the symbol “ $\otimes$ ” denotes the Kronecker product (?),  $\mathbf{F}_{2Q}$  and  $\mathbf{F}_{2P}$  are the  $2Q \times 2Q$  and  $2P \times 2P$  unitary DFT matrices (?), p. 31), respectively, the superscript “ $*$ ” denotes the complex conjugate and  $\boldsymbol{\Lambda}$  is a  $4QP \times 4QP$  diagonal matrix containing the eigenvalues of  $\mathbf{C}$ . Due to the diagonalization of the matrix  $\mathbf{C}$ , the auxiliary system (equation 21) can be rewritten by using equation 22 and premultiplying both sides of the result by  $(\mathbf{F}_{2Q} \otimes \mathbf{F}_{2P})$ , i.e.,

$$\boldsymbol{\Lambda} (\mathbf{F}_{2Q} \otimes \mathbf{F}_{2P}) \mathbf{v} = (\mathbf{F}_{2Q} \otimes \mathbf{F}_{2P}) \mathbf{w}. \quad (23)$$

By applying the vec-operator (Takahashi et al., 2020) to both sides of equation 23, by premultiplying both sides of the result by  $\mathbf{F}_{2Q}^*$  and then postmultiplying both sides of the result by  $\mathbf{F}_{2P}^*$

$$\mathbf{F}_{2Q}^* [\mathbf{L} \circ (\mathbf{F}_{2Q} \mathbf{V} \mathbf{F}_{2P})] \mathbf{F}_{2P}^* = \mathbf{W}, \quad (24)$$

368 where “ $\circ$ ” denotes the Hadamard product (? , p. 298) and  $\mathbf{L}$ ,  $\mathbf{V}$  and  $\mathbf{W}$  are  $2Q \times 2P$  matrices obtained  
 369 by rearranging, along their rows, the elements forming the diagonal of matrix  $\Lambda$ , vector  $\mathbf{v}$  and vector  $\mathbf{w}$ ,  
 370 respectively. The left side of equation 24 contains the 2D Inverse Discrete Fourier Transform (IDFT) of the  
 371 term in brackets, which in turn represents the Hadamard product of matrix  $\mathbf{L}$  and the 2D DFT of matrix  $\mathbf{V}$ .  
 372 Matrix  $\mathbf{L}$  contains the eigenvalues of  $\Lambda$  (equation 22) and can be efficiently computed by using only the  
 373 first column of the BCCB matrix  $\mathbf{C}$  (equation 21).

374 Actually, in Takahashi et al. (2020, 2022) a fast 2D discrete circular convolution (?) is used to process  
 375 very large gravity and magnetic datasets efficiently. The convolutional equivalent layer was applied to  
 376 perform upward continuation of large magnetic datasets. Compared to the classical Fourier approach,  
 377 Takahashi et al.’s (2022) method produces smaller border effects without using any padding scheme.

378 Without taking advantage of the symmetric BTTB structure of the sensitivity matrix (Takahashi et al.,  
 379 2020) that arises when gravimetric observations are measured on a horizontally regular grid, on a flat  
 380 surface and considering a regular grid of equivalent sources whithin a horizontal layer, Mendonça (2020)  
 381 explored the symmetry of the gravity kernel to reduce the number of forward model evaluations. By  
 382 exploting the symmetries of the gravity kernels and redundancies in the forward model evaluations on a  
 383 regular grid and combining the subspace solution based on eigenvectors of the gridded dataset, Mendonça  
 384 (2020) estimated the mass excess or deficiency produced by anomalous sources with positive or negative  
 385 density contrast.

### 386 2.2.8 The deconvolutional equivalent layer with BTTB matrices

387 To avoid the iterations of the conjugate gradient method in Takahashi et al. (2022), we can employ the  
 388 deconvolution process. Equation 24 shows that estimate the matrix  $\mathbf{V}$ , containing the elements of parameter  
 389 vector  $\mathbf{p}$ , is a inverse problem that could be solved by deconvolution. From equation 24, the matrix  $\mathbf{V}$  can  
 390 be obtain by deconvolution, i.e.

$$\mathbf{V} = \mathbf{F}_{2Q}^* \left[ \frac{(\mathbf{F}_{2Q} \mathbf{W} \mathbf{F}_{2P})}{\mathbf{L}} \right] \mathbf{F}_{2P}^*. \quad (25)$$

391 Equation 25 shows that the parameter vector (in matrix  $\mathbf{V}$ ) can be theoretically obtain by dividing each  
 392 potential-field observations (in matrix  $\mathbf{W}$ ) by each eigenvalues (in matrix  $\mathbf{L}$ ). Hence, the parameter vector  
 393 is constructed by element-by-element division of data by eigenvalues.

394 However, the deconvolution often is extremely unstable. This means that a small change in data can lead  
 395 to an enormous change in the estimated parameter. Hence, equation 25 requires regularization to be useful.  
 396 We usede wiener deconvolution to obtain a stable solution, i.e.,

$$\mathbf{V} = \mathbf{F}_{2Q}^* \left[ (\mathbf{F}_{2Q} \mathbf{W} \mathbf{F}_{2P}) \frac{\mathbf{L}^*}{(\mathbf{L} \mathbf{L}^* + \mu)} \right] \mathbf{F}_{2P}^*, \quad (26)$$

397 where the matrix  $\mathbf{L}^*$  contains the complex conjugate eigenvalues and  $\mu$  is a parameter that controls the  
 398 degree of stabilization.

### 399 2.3 Solution stability

400 The solution stability of the equivalent-layer methods is rarely addressed. Here, we follow the numerical  
 401 stability analysis presented in Siqueira et al. (2017).

402 Let us assume noise-free potential-field data  $\mathbf{d}$ , we estimate a physical-property distribution  $\mathbf{p}$  (estimated  
 403 solution) within the equivalent layer. Then, the noise-free data  $\mathbf{d}$  are contaminated with additive  $D$  different  
 404 sequences of pseudorandom Gaussian noise, creating different noise-corrupted potential-field data  $\mathbf{d}_\ell^o$ ,  
 405  $\ell = 1, \dots, D$ . From each  $\mathbf{d}_\ell^o$ , we estimate a physical-property distribution  $\hat{\mathbf{p}}_\ell$  within the equivalent layer.

406 Next, for each noise-corrupted data  $\mathbf{d}_\ell^o$  and estimated solution  $\hat{\mathbf{p}}_\ell$ , the  $\ell$ th model perturbation  $\delta p_\ell$  and the  
 407  $\ell$ th data perturbation  $\delta d_\ell$  are, respectively, evaluated by

$$\delta p_\ell = \frac{\|\hat{\mathbf{p}}_\ell - \mathbf{p}\|_2}{\|\mathbf{p}\|_2}, \quad \ell = 1, \dots, D, \quad (27)$$

408 and

$$\delta d_\ell = \frac{\|\mathbf{d}_\ell^o - \mathbf{d}\|_2}{\|\mathbf{d}\|_2}, \quad \ell = 1, \dots, D. \quad (28)$$

409 Regardless of the particular method used, the following inequality (Aster et al., 2018, p. 66) is applicable:

$$\delta p_\ell \leq \kappa \delta d_\ell, \quad \ell = 1, \dots, D, \quad (29)$$

410 where  $\kappa$  is the constant of proportionality between the model perturbation  $\delta p_\ell$  (equation 27) and the data  
 411 perturbation  $\delta d_\ell$  (equation 28). The constant  $\kappa$  acts as the condition number of an invertible matrix in a  
 412 given inversion, and thus measures the instability of the solution. The larger (smaller) the value of  $\kappa$  the  
 413 more unstable (stable) is the estimated solution.

414 Equation 29 shows a linear relationship between the model perturbation and the data perturbation. By  
 415 plotting  $\delta p_\ell$  (equation 27) against  $\delta d_\ell$  (equation 28) produced by a set of  $D$  estimated solution obtained by  
 416 applying a given equivalent-layer method, we obtain a straight line behaviour described by equation 29.  
 417 By applying a linear regression, we obtain a fitted straight line whose estimated slope ( $\kappa$  in equation 29)  
 418 quantifies the solution stability.

419 Here, the analysis of solution stability is numerically conducted by applying the classical equivalent-  
 420 layer technique with zeroth-order Tikhonov regularization, the convolutional method for gravimetric and  
 421 magnetic data, the deconvolutional method (equation 25) and the deconvolutional method with different  
 422 values for the Wiener stabilization (equation 26).

### 3 NUMERICAL SIMULATIONS

423 We investigated different computational algorithms for inverting gravity disturbances and total-field  
 424 anomalies. To test the capability of the fast equivalent-layer technique for processing that potential field  
 425 data we measure of the computational effort by counting the number of floating-point operations (*flops*),  
 426 such as additions, subtractions, multiplications, and divisions (Golub and Loan, 2013) for different number  
 427 of observation points, ranging from 10, 000 up to 1, 000, 000. The results generated when using iterative  
 428 methods are set to  $it = 50$  for the number of iterations.

429 **3.1 Floating-point operations calculation**

430 To measure the computational effort of the different algorithms to solve the equivalent layer linear system,  
 431 a non-hardware dependent method can be useful because allow us to do direct comparison between them.  
 432 Counting the floating-point operations (*flops*), i.e., additions, subtractions, multiplications and divisions is  
 433 a good way to quantify the amount of work of a given algorithm (Golub and Loan, 2013). For example, the  
 434 number of *flops* necessary to multiply two vectors  $\mathbb{R}^N$  is  $2N$ . A common matrix-vector multiplication with  
 435 dimension  $\mathbb{R}^{N \times N}$  and  $\mathbb{R}^N$ , respectively, is  $2N^2$  and a multiplication of two matrices  $\mathbb{R}^{N \times N}$  is  $2N^3$ . Figure  
 436 1 shows the total flops count for the different methods presented in this review with a crescent number of  
 437 data, ranging from 10, 000 to 1, 000, 000 for the gravity equivalent layer and figure 2 for magnetic data.

438 **3.1.1 Normal equations using Cholesky decomposition**

439 The equivalent sources can be estimated directly from solving the normal equations 1. In this work we  
 440 will use the Cholesky decompositions method to calculate the necessary *flops*. In this method it is calculated  
 441 the lower triangule of  $\mathbf{A}^T \mathbf{A}$  ( $1/2N^3$ ), the Cholesky factor ( $1/3N^3$ ), a matrix-vector multiplication ( $2N^2$ )  
 442 and finally solving the triangular system ( $2N^2$ ), totalizing

$$f_{classical} = \frac{5}{6}N^3 + 4N^2 \quad (30)$$

443 **3.1.2 Window method (Leão and Silva, 1989)**

444 The moving data-window scheme (Leão and Silva, 1989) solve  $N$  linear systems with much smaller sizes.  
 445 For our results we are considering a data-window of the same size of which the authors presented in theirs  
 446 work ( $N_w = 49$ ) and the same number of equivalent sources ( $M_w = 225$ ). We are doing this process for all  
 447 the other techniques to standardize the resolution of our problem. Using the Cholesky decomposition with  
 448 this method the *flops* are

$$f_{window} = N \frac{5}{6} M_w N_w^2 + 4N_w M_w \quad (31)$$

449 **3.1.3 PEL method (Oliveira Jr. et al., 2013)**

450 The polynomial equivalent layer uses a similar approach of moving windows from Leão and Silva  
 451 (1989). For this operations calculation we used a first degree polynomial (three variables) and each window  
 452 contains 1, 000 observed data ( $N_s$ ). Following the steps given in (Oliveira Jr. et al., 2013) the total *flops*  
 453 becomes

$$f_{pel} = \frac{1}{3}H^3 + 2H^2 + 2NN_wH + H^2N + 2HN + 2NP \quad (32)$$

454 where  $H$  is the number of variable of the polynomial times the number of windows ( $3 \times N/1000$ ).

#### 455 3.1.4 Conjugate gradient least square (CGLS)

456 The CGLS method is a very stable and fast algorithm for solving linear systems iteratively. Its computational  
 457 complexity envolves a matrix-vector product outside the loop ( $2N^2$ ), two matrix-vector products  
 458 inside the loop ( $4N^2$ ) and six vector products inside the loop ( $12N$ ) (Aster et al., 2018)

$$f_{ccls} = 2N^2 + it(4N^2 + 12N) \quad (33)$$

#### 459 3.1.5 Wavelet compression method with CGLS (Li and Oldenburg, 2010)

460 For the wavelet method we have calculated a cocompression rate of 98% ( $C_r = 0.2$ ) for the threshold  
 461 as the authors in Li and Oldenburg (2010) used and the wavelet transformation requiring  $\log_2(N)$  flops  
 462 each, with its inverse also using the same number of operations. Combined with the conjugate gradient  
 463 least square necessary steps and iterations, the number of flops are

$$f_{wavelet} = 2NC_r + 4N\log_2(N) + it(4N\log_2(N) + 4NC_r + 12C_r) \quad (34)$$

#### 464 3.1.6 Fast equivalent layer for gravity data (Siqueira et al., 2017)

465 The fast equivalent layer from Siqueira et al. (2017) solves the linear system in  $it$  iterations. The main  
 466 cost of this method is the matrix-vector multiplication to asses the predicted data ( $2N^2$ ) and three simply  
 467 element by element vector sum, subtraction and division ( $3N$  total)

$$f_{siqueira} = it(3N + 2N^2) \quad (35)$$

#### 468 3.1.7 Convolutional equivalent layer for gravity data (Takahashi et al., 2020)

469 This methods replaces the matrix-vector multiplication of the iterative fast-equivalent technique (Siqueira  
 470 et al., 2017) by three steps involving a Fourier transform and a inverse Fourier transform, and a Hadamard  
 471 product of matrices. Considering that the first column of our BCCB matrix has  $4N$  elements, the flops  
 472 count of this method is

$$f_{convgrav} = \kappa 4N \log_2(4N) + it(27N + \kappa 8N \log_2(4N)) \quad (36)$$

473 In the resultant count we considered a radix-2 algorithm for the fast Fourier transform and its inverse,  
 474 which has a  $\kappa$  equals to 5 and requires  $\kappa 4N \log_2(4N)$  flops each. The Hadarmard product of two matrices  
 475 of  $4N$  elements with complex numbers takes  $24N$  flops. Note that equation 36 is different from the one  
 476 presented in Takahashi et al. (2020) because we also added the flops necessary to calculate the eigenvalues  
 477 in this form. It does not differentiate much in order of magnitude because the iterative part is the most  
 478 costful.

## 479 3.1.8 Convolutional equivalent layer for magnetic data (Takahashi et al., 2022)

480 The convolutional equivalent layer for magnetic data uses the same flops count of the main operations as  
481 in the gravimetric case, the big difference is the use of the conjugate gradient algorithm to solve the inverse  
482 problem. It requires a Hadamard product outside of the iterative loop and more matrix-vector vector-vector  
483 multiplications inside the loop as seem in equation 33.

$$f_{convmag} = \kappa 16N \log_2(4N) + 24N + it(\kappa 16N \log_2(4N) + 60N) \quad (37)$$

## 484 3.1.9 Deconvolutional method

485 The deconvolution method does not require an iterative algorithm, rather it solves the estimative of the  
486 physical properties in a single step using the  $4N$  eigenvalues of the BCCB matrix as in the convolutional  
487 method. It requires a two fast Fourier transform ( $\kappa 4N \log_2(4N)$ ), one for the eigenvalues and another for  
488 the data transformation, a element by element division ( $24N$ ) and finally, a fast inverse Fourier transform  
489 for the final estimative ( $\kappa 4N \log_2(4N)$ ).

$$f_{deconv} = \kappa 12N \log_2(4N) + 24N \quad (38)$$

490 Using the deconvolutional method with a Wiener stabilization adds two multiplications of complex  
491 elements of the conjugates eigenvalues ( $24N$  each) and the sum of  $4N$  elements with the stabilization  
492 parameter  $\mu$

$$f_{deconvwiener} = \kappa 12N \log_2(4N) + 76N \quad (39)$$

## 4 SYNTHETIC DATA SIMULATIONS

493 For all applications, we generate a model composed by two spheres (PAREI AQUI - ANDRE)  
 494 Grav: the prism has a contrast of density equal to  $550\text{kg/m}^3$ , the left sphere  $600\text{kg/m}^3$  and the right  
 495 sphere  $-500\text{kg/m}^3$   
 496 Mag: all 3 bodies have magnetization of 3.46 intensity, 35.26 declination and 45.0 inclinations. The grid  
 497 of the synthetic data is 50x50.

### 4.1 Stability analysis

499 For the stability analysis we show the comparison of the normal equations solution with zeroth-order  
 500 Tikhonov regularization, the convolutional method for gravimetric and magnetic data, the deconvolutional  
 501 method and the deconvolutional method with different values for the Wiener stabilization. We create 21  
 502 data sets adding a crescent pseudo-random noise to the original data, which varies from 0% to 10% of  
 503 the maximum anomaly value, in intervals of 0.5%. These noises has mean equal to zero and a Gaussian  
 504 distribution. Figure XX shows how the residual between the predicted data and the noise-free data changes  
 505 as the level of the noise is increased. We can see that for all methods, a linear tendency can be observed as  
 506 it is expected. The inclination of the straight line is a indicative of the stability of each method. As show  
 507 in the graph the deconvolutional method is very unstable and it is really necessary to use a stabilization  
 508 method to have a good parameter estimative. In contrast, a correct value of the stabilization parameter is  
 509 necessary to not overshoot the smoothness of the solution as it is the case for the well-known zeroth-order  
 510 Tikhonov regularization. For the example using this gravimetric data, the optimal value for the Wiener  
 511 stabilization parameter is  $\mu = 10^{-9}$ . Figure XX shows the comparison of the predicted data for each  
 512 method with the original data.

513 For the magnetic data, the Wiener parameter seems to have the best solution for  $\mu = 10^{-13}$ . Figure XX  
 514 shows the comparison of the predicted data for each method with the original data.

515 Gravity synthetic statistics to be included:

516 Means

517 0.24791339230971493 (Classical method)

518 0.25522040542133817 (CG BTTB method)

519 0.86010282709889 (Deconvolutional method)

520 1.53835137193657 (Deconvolutional w Wiener overshoot  $\mu$  method)

521 0.3134732823974472 (Deconvolutional w Wiener optimal  $\mu$  method)

522 0.5553048046997608 (Deconvolutional w Wiener suboptimal  $\mu$  method)

523 Standard deviations

524 0.18274083156485463 (Classical method)

525 0.18986126212291252 (CG BTTB method)

526 1.439293452270024 (Deconvolutional method)

527 1.1183051446613188 (Deconvolutional w Wiener overshoot  $\mu$  method)

528 0.2367045031838225 (Deconvolutional w Wiener optimal  $\mu$  method)

529 0.7047326489645682 (Deconvolutional w Wiener suboptimal  $\mu$  method)  
530  
531 Magnetic synthetic statistics to be included:  
532 Means  
533 4.71700586977892 (Classical method)  
534 4.791561788289162 (CG BTTB method)  
535 2761.170136908849 (Deconvolutional method)  
536 23.06442216727077 (Deconvolutional w Wiener overshoot  $\mu$  method)  
537 8.860326967314595 (Deconvolutional w Wiener optimal  $\mu$  method)  
538 33.83142137645327 (Deconvolutional w Wiener suboptimal  $\mu$  method)  
539 Standard deviations  
540 3.571868619217408 (Classical method)  
541 3.6420538498453263 (CG BTTB method)  
542 4507.745135864884 (Deconvolutional method)  
543 14.232818621809827 (Deconvolutional w Wiener overshoot  $\mu$  method)  
544 7.445085208152109 (Deconvolutional w Wiener optimal  $\mu$  method)  
545 47.8175518946965 (Deconvolutional w Wiener suboptimal  $\mu$  method)

## 5 REAL DATA APPLICATION

546 Gridded data of 1000x500 (500000 observed points) for both grav and mag. Data is at -900m.  
547 Grav equivalent layer depth is 300 m and 50 iterations of the cgls method was used. Mag equivalent layer  
548 depth is 0 m and 200 iterations of the cgls method was used.  
549 On an Intel Core i7 7700HQ@2.8 GHz processor in single processing and single-threading modes the  
550 gravimetric equivalent layer took 9.19 seconds to estimate the equivalent sources with the convolutional  
551 method and 0.51 seconds with the deconvolutional method.  
552 The magnetic equivalent layer took 82 seconds to estimate the equivalent sources with the convolutional  
553 method and 0.84 seconds with the deconvolutional method.  
554 As Carajás area is very large different values of the magnetic main field can be considered.  
555 The main field declination was calculated using the tool in the website (for the date 01/01/2014):  
556 <https://www.ngdc.noaa.gov/geomag/calculators/magcalc.shtml> For this application I considered an approxi-  
557 mated mid location of the area (latitude  $-6.55^\circ$  and longitude  $-50.75^\circ$ ). The declination is  $-19.865^\circ$   
558 and the inclination  $-7.43915^\circ$ . As the source magnetization is unknown inclination and declination equal  
559 to the main field is being used for all the equivalent sources.  
560 Gravimetric case:  
561 Means  
562 0.0005096975472675431 (convolutional method)  
563 0.4582999511463665 (deconvolutional method with wiener  $\mu = 10^{-22}$ )  
564 Standart deviations  
565 0.15492798729938298 (convolutional method)  
566 1.229507199000529 (deconvolutional method with wiener  $\mu = 10^{-22}$ )  
567  
568 Magnetic case:  
569 Means  
570 -0.06404347121632468 (convolutional method)  
571 18.992921718679344 (deconvolutional method with wiener  $\mu = 10^{-16}$ )  
572 Standart deviations  
573 1.9687559764381535 (convolutional method)  
574 33.641199020925924 (deconvolutional method with wiener  $\mu = 10^{-16}$ )

## 6 DISCUSSION AND CONCLUSION

## CONFLICT OF INTEREST STATEMENT

575 The authors declare that the research was conducted in the absence of any commercial or financial  
576 relationships that could be construed as a potential conflict of interest.

## AUTHOR CONTRIBUTIONS

577 The Author Contributions section is mandatory for all articles, including articles by sole authors. If an  
578 appropriate statement is not provided on submission, a standard one will be inserted during the production  
579 process. The Author Contributions statement must describe the contributions of individual authors referred  
580 to by their initials and, in doing so, all authors agree to be accountable for the content of the work. Please  
581 see here for full authorship criteria.

## FUNDING

582 Diego Takahashi was supported by a Post-doctoral scholarship from CNPq (grant 300809/2022-0) Valéria  
583 C.F. Barbosa was supported by fellowships from CNPq (grant 309624/2021-5) and FAPERJ (grant  
584 26/202.582/2019). Vanderlei C. Oliveira Jr. was supported by fellowships from CNPq (grant 315768/2020-  
585 7) and FAPERJ (grant E-26/202.729/2018).

## ACKNOWLEDGMENTS

586 We thank the Brazilian federal agencies CAPES, CNPq, state agency FAPERJ and Observatório Nacional  
587 research institute and Universidade do Estado do Rio de Janeiro.

## DATA AVAILABILITY STATEMENT

588 The datasets generated for this study can be found in the frontiers-paper Github repository link:  
589 <https://github.com/DiegoTaka/frontiers-paper>.

## REFERENCES

- 590 Aster, R. C., Borchers, B., and Thurber, C. H. (2018). *Parameter estimation and inverse problems*  
591 (Elsevier)
- 592 Barbosa, V. C. F., Silva, J. B., and Medeiros, W. E. (1997). Gravity inversion of basement relief using  
593 approximate equality constraints on depths. *Geophysics* 62, 1745–1757
- 594 Barnes, G. and Lumley, J. (2011). Processing gravity gradient data. *Geophysics* 76, I33–I47. doi:10.1190/  
595 1.3548548
- 596 Cordell, L. (1992). A scattered equivalent-source method for interpolation and gridding of potential-field  
597 data in three dimensions. *Geophysics* 57, 629–636
- 598 Dampney, C. N. G. (1969). The equivalent source technique. *Geophysics* 34, 39–53. doi:10.1190/1.  
599 1439996
- 600 Davis, K. and Li, Y. (2011). Fast solution of geophysical inversion using adaptive mesh, space-filling  
601 curves and wavelet compression. *Geophysical Journal International* 185, 157–166. doi:10.1111/j.  
602 1365-246X.2011.04929.x
- 603 Friedman, J. H. (2001). Greedy function approximation: a gradient boosting machine. *Annals of statistics* ,  
604 1189–1232

- 605 Friedman, J. H. (2002). Stochastic gradient boosting. *Computational statistics and data analysis* 38,  
606 367–378
- 607 Golub, G. H. and Loan, C. F. V. (2013). *Matrix Computations (Johns Hopkins Studies in the Mathematical  
608 Sciences)* (Johns Hopkins University Press), 4 edn.
- 609 Guspí, F. and Novara, I. (2009). Reduction to the pole and transformations of scattered magnetic data using  
610 newtonian equivalent sources. *Geophysics* 74, L67–L73
- 611 Jirigalatu, J. and Ebbing (2019). A fast equivalent source method for airborne gravity gradient data.  
612 *Geophysics* 84, G75–G82. doi:10.1190/GEO2018-0366.1
- 613 Kellogg, O. D. (1929). *Foundations of Potential Theory* (Frederick Ungar Publishing Company)
- 614 Kennett, B., Sambridge, M., and Williamson, P. (1988). Subspace methods for large inverse problems with  
615 multiple parameter classes. *Geophysical Journal International* 94, 237–247
- 616 Leão, J. W. D. and Silva, J. B. C. (1989). Discrete linear transformations of potential field data. *Geophysics*  
617 54, 497–507. doi:10.1190/1.1442676
- 618 Li, Y. and Oldenburg, D. W. (2010). Rapid construction of equivalent sources using wavelets. *Geophysics*  
619 75, L51–L59. doi:10.1190/1.3378764
- 620 Mendonça, C. A. (2020). Subspace method for solving large-scale equivalent layer and density mapping  
621 problems. *Geophysics* 85, G57–G68. doi:10.1190/geo2019-0302.1
- 622 Mendonça, C. A. and Silva, J. B. C. (1994). The equivalent data concept applied to the interpolation of  
623 potential field data. *Geophysics* 59, 722–732. doi:10.1190/1.1443630
- 624 Oldenburg, D., McGillivray, P., and Ellis, R. (1993). Generalized subspace methods for large-scale inverse  
625 problems. *Geophysical Journal International* 114, 12–20
- 626 Oliveira Jr., V. C., Barbosa, V. C. F., and Uieda, L. (2013). Polynomial equivalent layer. *Geophysics* 78,  
627 G1–G13. doi:10.1190/geo2012-0196.1
- 628 Siqueira, F. C., Oliveira Jr, V. C., and Barbosa, V. C. (2017). Fast iterative equivalent-layer technique for  
629 gravity data processing: A method grounded on excess mass constraint. *Geophysics* 82, G57–G69
- 630 Skilling, J. and Bryan, R. (1984). Maximum entropy image reconstruction-general algorithm. *Monthly  
631 Notices of the Royal Astronomical Society*, Vol. 211, NO. 1, P. 111, 1984 211, 111
- 632 Soler, S. R. and Uieda, L. (2021). Gradient-boosted equivalent sources. *Geophysical Journal International*  
633 227, 1768–1783. doi:10.1093/gji/ggab297
- 634 Takahashi, D., Oliveira, V. C., and Barbosa, V. C. (2022). Convolutional equivalent layer for magnetic data  
635 processing. *Geophysics* 87, 1–59
- 636 Takahashi, D., Oliveira Jr, V. C., and Barbosa, V. C. (2020). Convolutional equivalent layer for gravity data  
637 processing. *Geophysics* 85, G129–G141
- 638 Xia, J. and Sprowl, D. R. (1991). Correction of topographic distortion in gravity data. *Geophysics* 56,  
639 537–541
- 640 Xia, J., Sprowl, D. R., and Adkins-Helgeson, D. (1993). Correction of topographic distortions in potential-  
641 field data; a fast and accurate approach. *Geophysics* 58, 515–523. doi:10.1190/1.1443434

## 7 SUPPLEMENTARY TABLES AND FIGURES

### 642 7.1 Figures

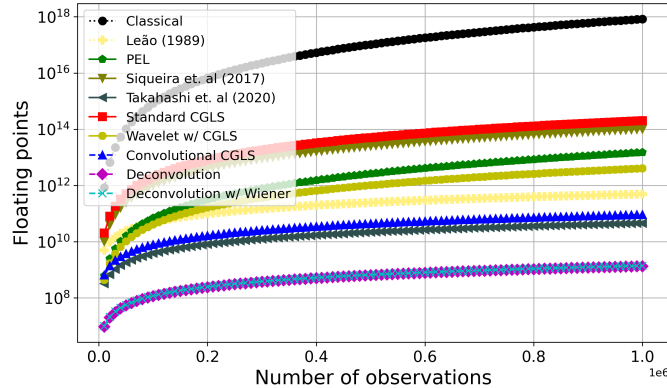


**Figure 1.** Number of *flops* for many of the methods described in this work to estimate the equivalent sources using gravity data. The range of observations varies from 10,000 to 1,000,000.

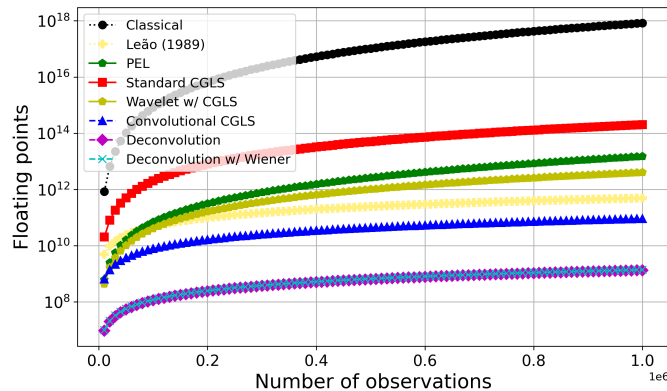


**Figure 2.** Number of *flops* for many of the methods described in this work to estimate the equivalent sources using magnetic data. The range of observations varies from 10,000 to 1,000,000.

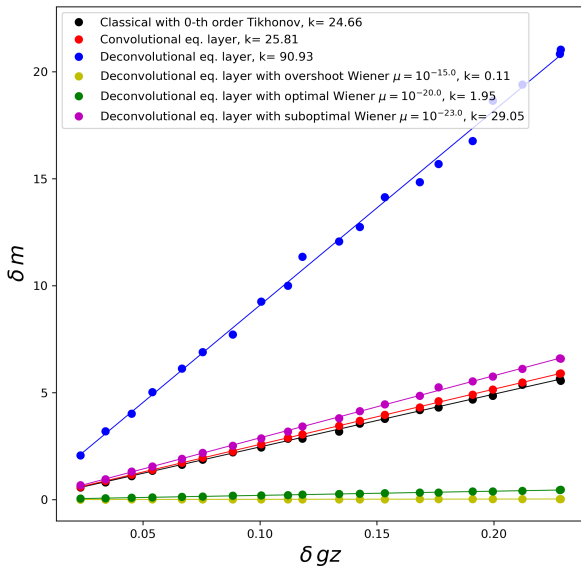


**Figure 3.** Stability analysis of some of the equivalent layer methods of the gravimetric case.

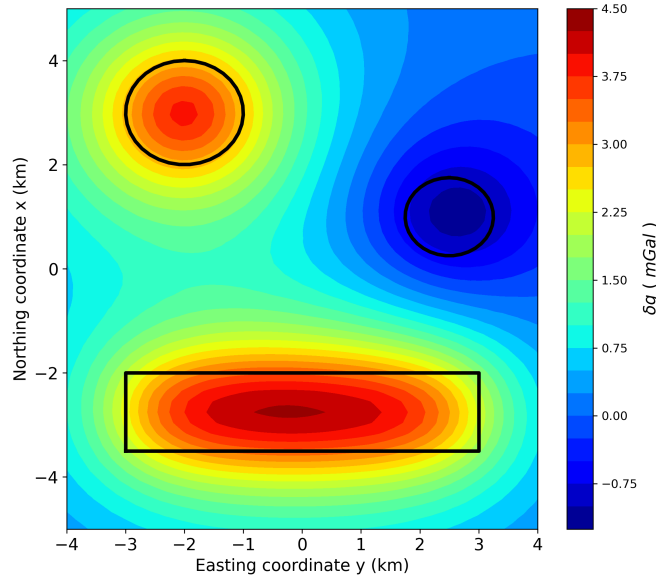


**Figure 4.** Synthetic noise-free data of the gravimetric case. The observations points and equivalent sources are placed in a regular grid of  $50 \times 50$ .

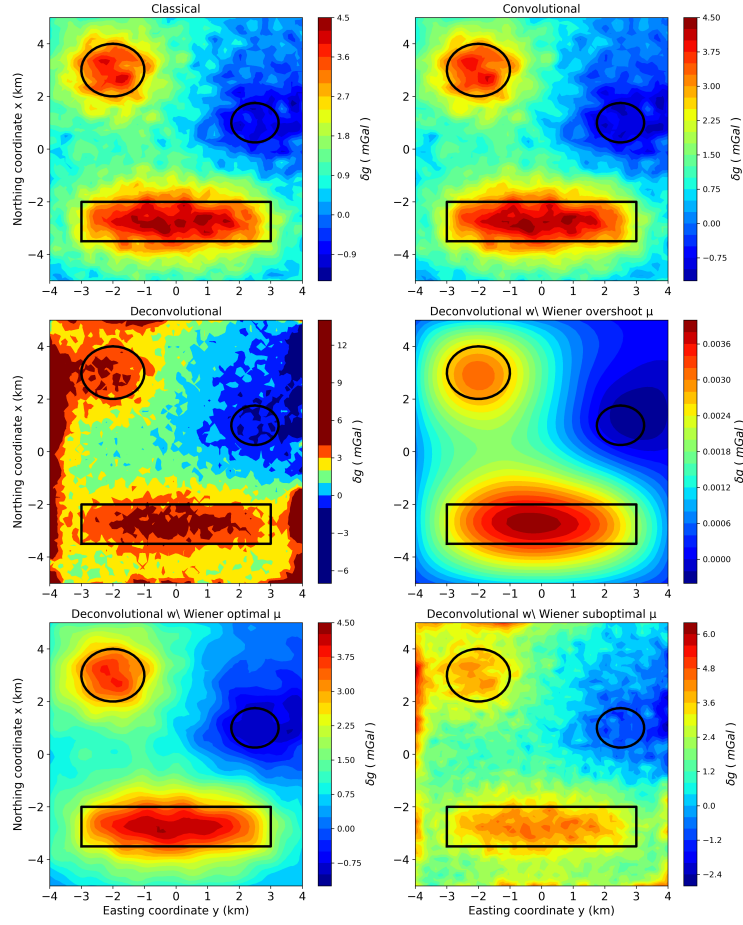


**Figure 5.** Predicted gravity data for different methods of the equivalent layer with maximum level of noise. Panel **(A)** is the classical method, **(B)** is the convolutional, **(C)** is the deconvolutional, **(D)** is the deconvolutional method using Wiener stabilization with a too high value for  $\mu$ , **(E)** is the deconvolutional method using Wiener stabilization with a optimal value for  $\mu$  and **(F)** is the deconvolutional method using Wiener stabilization with a too low value for  $\mu$ .

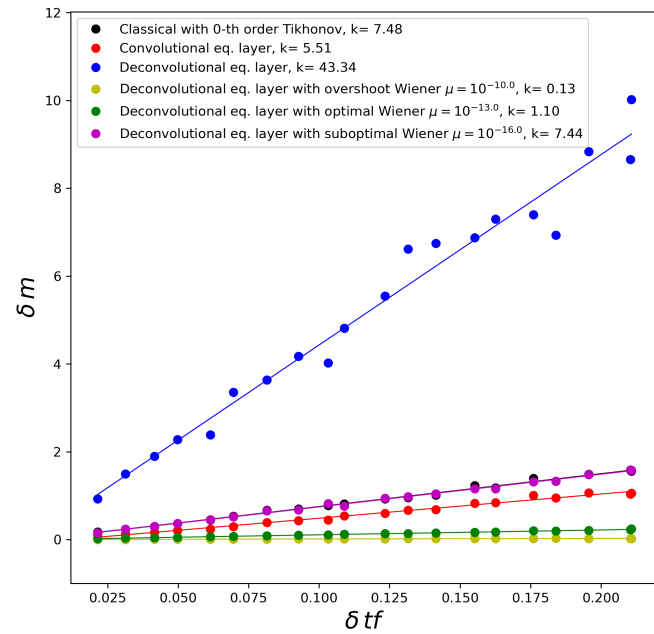


**Figure 6.** Stability analysis of some of the equivalent layer methods of the magnetic case.

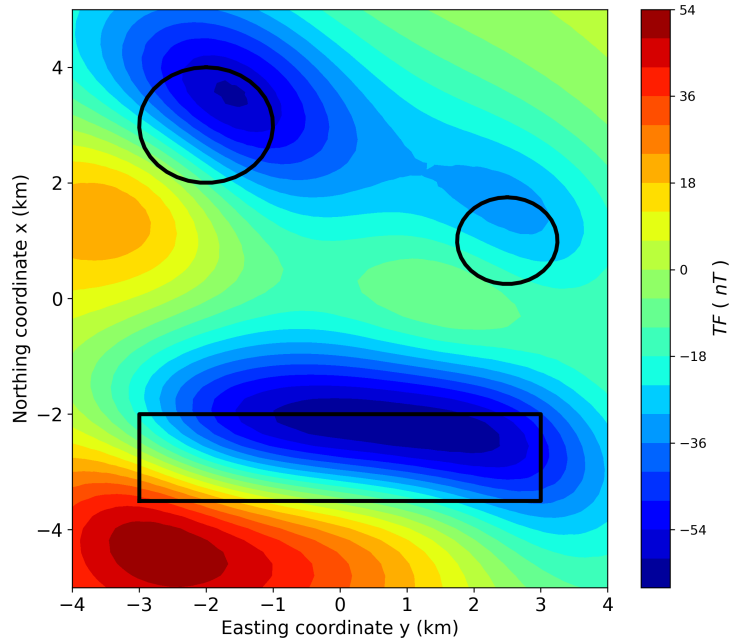


**Figure 7.** Synthetic noise-free data of the magnetic case. The observations points and equivalent sources are placed in a regular grid of  $50 \times 50$ .

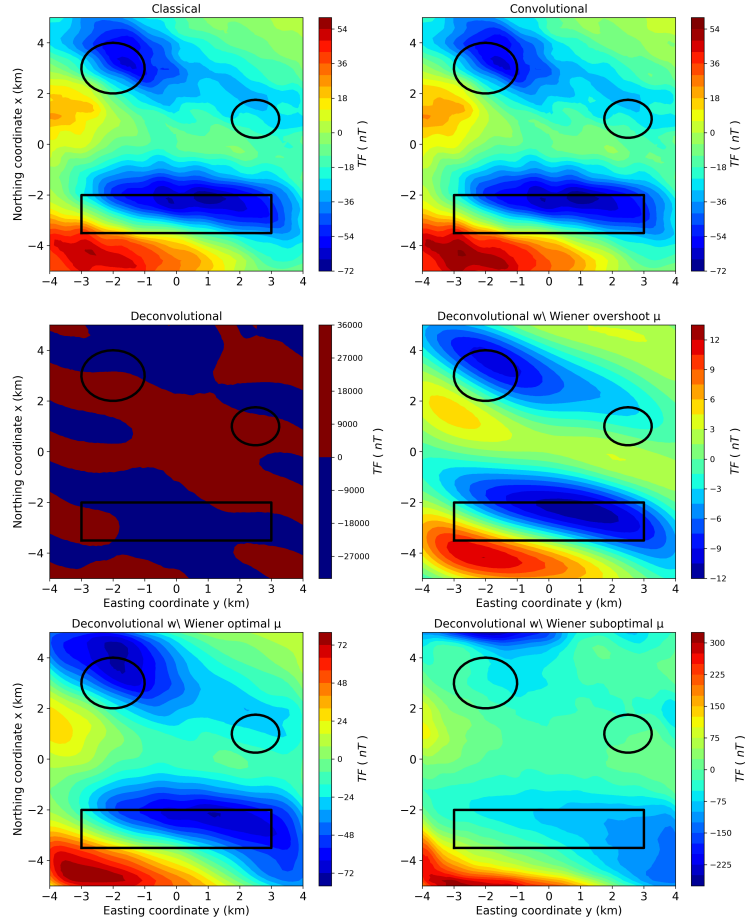


**Figure 8.** Predicted magnetic data for different methods of the equivalent layer with maximum level of noise. Panel **(A)** is the classical method, **(B)** is the convolutional, **(C)** is the deconvolutional, **(D)** is the deconvolutional method using Wiener stabilization with a too high value for  $\mu$ , **(E)** is the deconvolutional method using Wiener stabilization with a optimal value for  $\mu$  and **(F)** is the deconvolutional method using Wiener stabilization with a too low value for  $\mu$ .

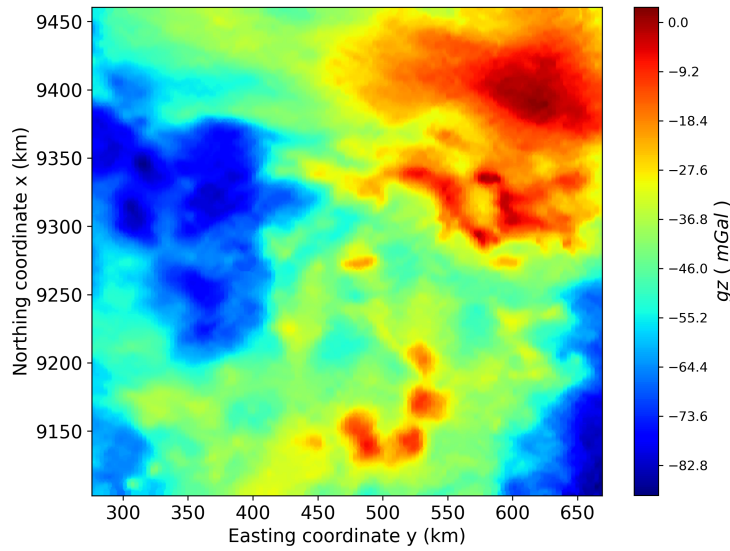


**Figure 9.** Gridded real aerogravimetric data from Carajás, Brazil. A regular grid of  $10,000 \times 500$  is being used, totalizing  $N, M = 5,000,000$  obsevation points and equivalent sources.

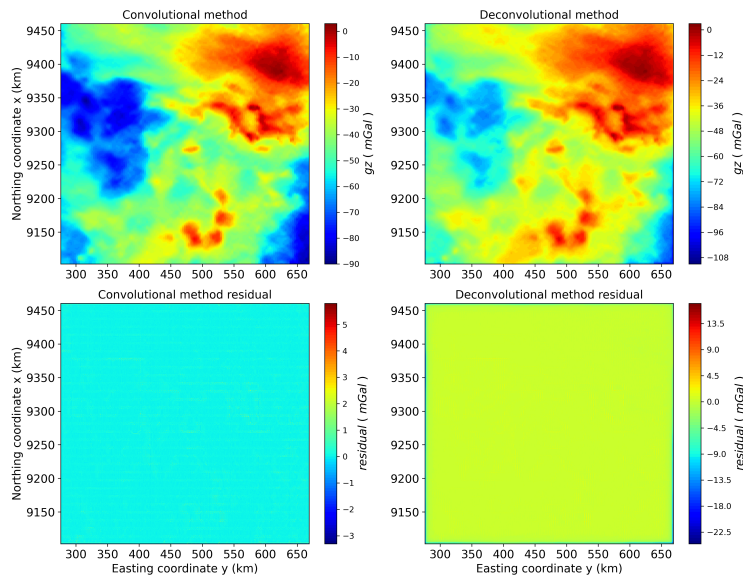


**Figure 10.** Panel (A) shows the predicted data from convolutional equivalent layer method. Panel (B) shows the residual from the convolutional equivalent layer method. Panel (C) shows the predicted data from deconvolutional equivalent layer method. Panel (D) shows the residual from the deconvolutional equivalent layer method.

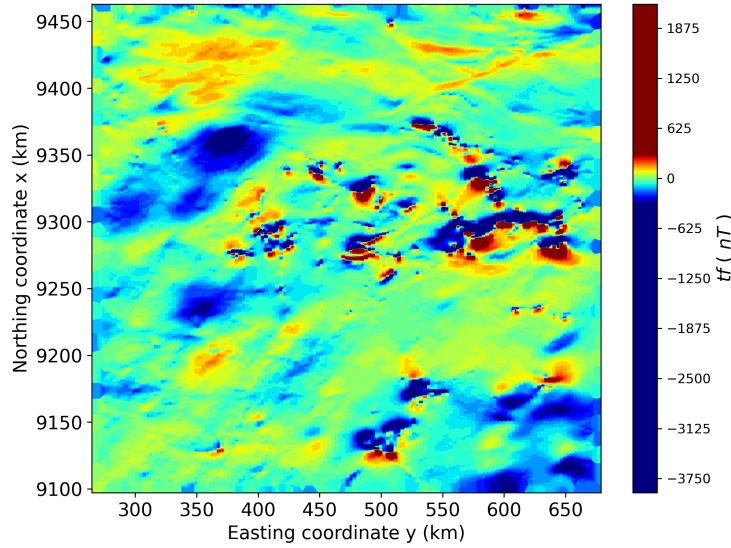


**Figure 11.** Gridded real aeromagnetic data from Carajás, Brazil. A regular grid of  $10,000 \times 500$  is being used, totalizing  $N, M = 5,000,000$  obsevation points and equivalent sources.

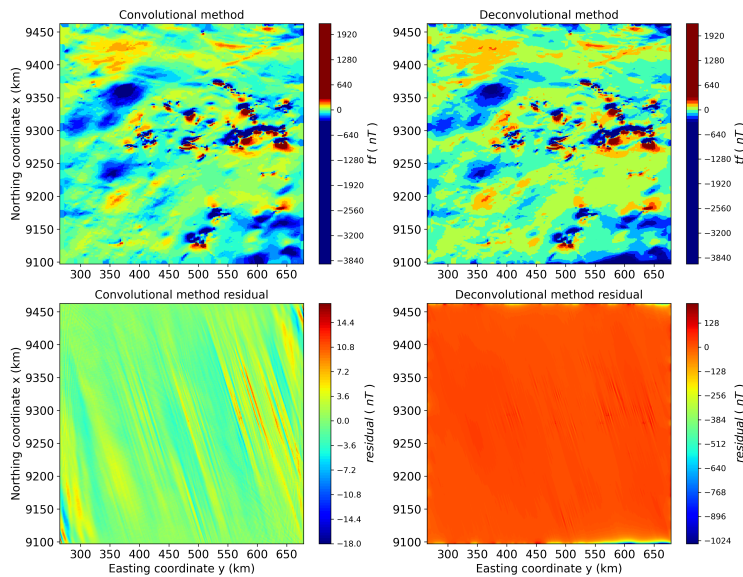


**Figure 12.** Panel (A) shows the predicted data from convolutional equivalent layer method. Panel (B) shows the residual from the convolutional equivalent layer method. Panel (C) shows the predicted data from deconvolutional equivalent layer method. Panel (D) shows the residual from the deconvolutional equivalent layer method.